Available online at www.sciencedirect.com
SCIENCE DIRECT®
Journal of Computational Physics 207 (2005) 588–609
JOURNAL OF COMPUTATIONAL PHYSICS
www.elsevier.com/locate/jcp

Three-dimensional bridging scale analysis of dynamic fracture

Harold S. Park [a,*], Eduard G. Karpov [b], Patrick A. Klein [a], Wing Kam Liu [b]

[a] *Sandia National Laboratories, Science-Based Material Modeling Department, Livermore, CA 94551, USA*
[b] *Department of Mechanical Engineering, Northwestern University, Evanston, IL 60208, USA*

Received 3 September 2004; received in revised form 17 December 2004; accepted 31 January 2005
Available online 17 March 2005

Abstract

This paper presents a three-dimensional generalization of the bridging scale concurrent method, a finite temperature multiple scale method that couples molecular dynamics (MD) to finite elements (FE). The generalizations include the numerical calculation of the boundary condition acting upon the reduced MD region, as such boundary conditions are analytically intractable for realistic three-dimensional crystal structures. The formulation retains key advantages emphasized in previous papers, particularly the compact size of the resulting time history kernel matrix. The coupled FE and reduced MD equations of motion are used to analyze dynamic fracture in a three-dimensional FCC lattice, where interesting physical phenomena such as crack branching are seen. The multiple scale results are further compared to benchmark MD simulations for verification purposes.

Keywords: Multiple scale simulations; Bridging scale; Coupling methods; Molecular dynamics; Finite elements; Dynamic fracture; Generalized Langevin equation

1. Introduction

Multiple scale methods have gained much interest lately for the potential offered in the direct numerical coupling of disparate length and time scales. It is envisaged that multiple scale simulations offer the best hope, for example, in extracting material properties directly using first principles atomistic simulations, while linking that information to successively larger length scales until structural material properties of interest can be established. In particular, the evaluation of these properties at or near material failure is an area of much interest.

* Corresponding author. Tel.: +1 847 644 7779; fax: +1 847 491 3915.
E-mail addresses: hpark@alumni.northwestern.edu (H.S. Park), w-liu@northwestern.edu (W.K. Liu).

0021-9991/$ - see front matter
doi:10.1016/j.jcp.2005.01.028

The end goal of this research is to develop predictive simulation capabilities that are capable of resolving patterns of deformation across distinct length scales, while utilizing that information to understand and predict material failure at a structural level. Breakthroughs in this field of research could have a hugely beneficial impact on the materials design and computer aided design communities. Considerable research on this, and other important scientific advances that may be possible using multiple scale methods are currently under way. Here, we offer a brief review of the methods developed towards this goal.

Many methods have been developed to couple atomistic-level simulations to continuum-level simulations. Two such methods are the quasicontinuum (QC) approach of Tadmor et al. [1], and the MAAD (macroscopic, atomistic, ab initio dynamics) approach of Abraham et al. [2]. Other interesting approaches have been recently developed, notably the coupled atomistic discrete dislocation (CADD) approach of Shilkrot et al. [3], the bridging domain method of Xiao and Belytschko [4], and the coarse-grained molecular dynamics (CGMD) approach of Rudd and Broughton [5]. As the present article is not intended as an exhaustive review, the interested reader is referred to the multiple scale review papers of Liu et al. [6], and Curtin and Miller [7].

Recently, the bridging scale was proposed by Wagner and Liu [8] to concurrently couple molecular dynamics (MD) and finite elements (FE); the development and application of the method in two-dimensions was shown in the recent work of Park et al. [9]. Important advantages of the bridging scale as compared to previous methods include the fact that the FE mesh need not be graded down to the atomic spacing, that different time steps can therefore be used for the MD and FE simulations, that a non-reflecting MD boundary condition can be formulated in terms of a lattice impedance force that augments the standard MD equations of motion, and finally that the bridging scale is valid for finite temperature, dynamic problems.

The focus of the current paper is a full generalization of the bridging scale to three dimensions, including the numerical calculation of the molecular dynamics boundary condition. As a result, a time history kernel matrix similar in form to the damping kernels of Adelman and Doll [10], Cai et al. [11], and E and Huang [12] is found. More specifically, the time history kernel found in this work is a multiple scale generalization of the single scale works of Wagner et al. [13], Karpov et al. [14,15], and Park et al. [16].

The time history kernel matrix in this work offers numerous advantages to previous work, namely the compact size of the matrix, the fact that the matrix can be calculated using an automated numerical procedure involving only standard Laplace and Fourier transform techniques, and the fact that only the force constants describing the interaction of a unit cell with its neighboring unit cells are needed before the automated numerical procedure can proceed. Furthermore, this time history kernel is a part of an MD and FE solution-dependent impedance force which augments the standard MD equation of motion. This leads naturally to a truly two-way coupled MD boundary condition, in which long wavelengths coming from the continuum are transferred to the MD region, while high frequency MD wavelengths that cannot be represented by the continuum are dissipated away.

The layout of this paper is as follows. We first develop the coupled MD and FE equations of motion, then motivate the need to eliminate the atomistics from large parts of the domain. We then provide the derivation by which the time history kernel representing the effects of the eliminated fine scale degrees of freedom upon the reduced atomic lattice can be found. The numerical examples utilize the numerically calculated time history kernel to study dynamic fracture in three dimensions using the bridging scale. Finally, concluding remarks are made, and future research directions are discussed.

2. Bridging scale fundamentals

In this section, we briefly present the bridging scale fundamentals. As much of the following material has been derived in previous works [8,17,9], we refer the interested reader to those works for complete detail.

Other applications of the bridging scale can be found in [18–23]. The fundamental idea is to decompose the total displacement field $\mathbf{u}(\mathbf{x})$ into coarse and fine scales

$$\mathbf{u}(\mathbf{x}) = \bar{\mathbf{u}}(\mathbf{x}) + \mathbf{u}'(\mathbf{x}), \tag{1}$$

where the total displacement $\mathbf{u}(\mathbf{x})$ is defined at all n_a atomic positions. For consistency, Greek indices (α, $\beta,\ldots$) will define atoms for the remainder of this paper, and uppercase Roman indices ($I,J,\ldots$) will define coarse scale nodes. The coarse scale is defined to be

$$\bar{\mathbf{u}}(\mathbf{X}_\alpha) = \sum_I N_I^\alpha \mathbf{d}_I. \tag{2}$$

Here, $N_I^\alpha = N_I(\mathbf{X}_\alpha)$ is the shape function of node I evaluated at the initial atomic position $\mathbf{X}_\alpha$, and $\mathbf{d}_I$ is the FE nodal displacement associated with node I. The summation in (2) is over all n_c coarse scale nodes in the domain, as are all such summations in this section.

At this point, it is convenient to employ a matrix representation for subsequent developments. The column vector $\mathbf{u}$ contains all spatial components of the total displacement at each atom, while the column vector $\mathbf{d}$ contains all spatial components of the coarse scale displacement at each node, i.e.

$$\mathbf{u} = \begin{pmatrix} u_{1x} \\ u_{1y} \\ u_{1z} \\ u_{2x} \\ \vdots \\ \vdots \\ u_{n_a z} \end{pmatrix}, \quad \mathbf{d} = \begin{pmatrix} d_{1x} \\ d_{1y} \\ d_{1z} \\ \vdots \\ d_{n_c z} \end{pmatrix}. \tag{3}$$

In (3), u_{1y} is the y component of $\mathbf{u}(X_1)$. The size of $\mathbf{u}$ is then $3n_a \times 1$, while the size of $\mathbf{d}$ is $3n_c \times 1$. Eq. (2) can then be written in matrix form as

$$\bar{\mathbf{u}} = \mathbf{N}\mathbf{d}, \tag{4}$$

where $\mathbf{N}$ is a matrix containing the FE shape functions evaluated at each initial atomic position $\mathbf{X}_\alpha$, and whose size is $3n_a \times 3n_c$. Note that this implies that the coarse scale solution $\bar{\mathbf{u}}$ is also defined at every atomic position.

The fine scale is defined to be the projection of the MD displacements $\mathbf{q}$ onto the FE basis functions subtracted from the total solution $\mathbf{u}$, which is equivalent to the MD displacements $\mathbf{q}$. In other words, the fine scale represents that part of the total solution that the coarse scale cannot represent,

$$\mathbf{u}' = \mathbf{q} - \mathbf{P}\mathbf{q}, \tag{5}$$

where the projection matrix $\mathbf{P}$ is defined to be

$$\mathbf{P} = \mathbf{N}\mathbf{M}^{-1}\mathbf{N}^{\mathrm{T}}\mathbf{M}_A. \tag{6}$$

In (6), $\mathbf{M}_A$ is a diagonal matrix of size $3n_a \times 3n_a$ with the atomic masses on the diagonal and $\mathbf{M} = \mathbf{N}^{\mathrm{T}}\mathbf{M}_A\mathbf{N}$ is the coarse scale mass matrix of size $3n_c \times 3n_c$. We note that $\mathbf{P}$ satisfies the definition of a projection matrix, i.e. $\mathbf{PP} = \mathbf{P}$. The total displacement $\mathbf{u}$ can finally be written as the sum of the coarse and fine scales as

$$\mathbf{u} = \mathbf{N}\mathbf{d} + \mathbf{q} - \mathbf{P}\mathbf{q}. \tag{7}$$

The final term in the above equation is called the bridging scale. It is the part of the solution that must be removed from the total displacement so that a complete separation of scales is achieved, i.e., the coarse and fine scales are orthogonal, or linearly independent of each other.

The coupled MD and FE equations of motion are derived using (7) by first constructing a multi-scale Lagrangian L, which is defined to be the kinetic energy minus the potential energy

$$L(\mathbf{u}, \dot{\mathbf{u}}) = \mathscr{K}(\dot{\mathbf{u}}) - V(\mathbf{u}). \tag{8}$$

The coupled multi-scale equations of motion are obtained from the Lagrangian by following the relations

$$\frac{\mathrm{d}}{\mathrm{d}t}\left(\frac{\partial L}{\partial \dot{\mathbf{d}}}\right) - \frac{\partial L}{\partial \mathbf{d}} = 0, \tag{9}$$

$$\frac{\mathrm{d}}{\mathrm{d}t}\left(\frac{\partial L}{\partial \dot{\mathbf{q}}}\right) - \frac{\partial L}{\partial \mathbf{q}} = 0. \tag{10}$$

The coupled equations of motion can finally be written as:

$$\mathbf{M}_A\ddot{\mathbf{q}} = \mathbf{f}, \tag{11}$$

$$\mathbf{M}\ddot{\mathbf{d}} = \mathbf{N}^{\mathrm{T}}\mathbf{f}(\mathbf{u}). \tag{12}$$

Now that the coupled coarse and fine scale equations of motion have been derived, we make some brief comments:

(i) The fine scale equation (11) is simply the MD equation of motion. Therefore, a standard MD solver can be used to obtain the MD displacements $\mathbf{q}$, while the MD forces $\mathbf{f}$ can be found using any relevant potential energy function.

(ii) The coarse scale equation (12) is simply the FE equation of motion. Thus, we can use standard finite element methods to find the solution to (12), while noting that the finite element mass matrix $\mathbf{M}$ is defined to be a consistent mass matrix.

(iii) The coupling between the two equations is through the coarse scale internal force $\mathbf{N}^{\mathrm{T}}\mathbf{f}(\mathbf{u})$, which is a direct function of the MD internal force $\mathbf{f}$. In the region in which MD exists, the coarse scale force is calculated by extrapolating the MD force by way of the finite element shape functions $\mathbf{N}$. The MD forces can therefore be thought of as defining the constitutive relation for the finite element internal force.

(iv) The FE equation of motion is redundant for the case in which the MD and FE regions both exist everywhere in the domain, because the FE equation of motion is simply an approximation to the MD equation of motion, with the quality of the approximation governed by the finite element shape functions $\mathbf{N}$. We note that due to the kronecker-delta property of the finite element shape functions, the coarse scale internal force $\mathbf{N}^{\mathrm{T}}\mathbf{f}(\mathbf{u})$ *exactly* reduces to the MD forces for the case in which the finite element nodes coexist with atomic positions. We shall remove this redundancy in the next section, when we create coupled MD and FE equations of motion for systems where the MD region is confined to a small portion of the domain.

(v) The total solution $\mathbf{u}$ satisfies the same equation of motion as $\mathbf{q}$, i.e.

$$\mathbf{M}_A\ddot{\mathbf{u}} = \mathbf{f}. \tag{13}$$

This result is due to the fact that $\mathbf{q}$ and $\mathbf{u}$ satisfy the same initial conditions, and will be utilized in deriving the boundary conditions on the MD simulation in the following section.

(vi) Because of the equality of $\mathbf{q}$ and $\mathbf{u}$, it would appear that solving the FE equation of motion is unnecessary, since the coarse scale can be calculated directly using (7) as the projection of $\mathbf{q}$, i.e. $\mathbf{Nd} = \mathbf{Pq}$. However, because the fine scale will be eliminated from large portions of the domain in the following section, the MD displacements $\mathbf{q}$ are not defined over the entire domain, and thus it is not possible to calculate the coarse scale solution everywhere via direct projection of the MD displacements. Therefore, the solution of the FE equation of motion everywhere ensures a continuous coarse scale displacement field.

3. MD impedance boundary condition

3.1. Linearized fine scale equation of motion

In the bridging scale approach to multiple scale modeling, we assume that the atomistic domain can be decomposed into two distinct regions. The first region consists of cracks, lattice defects and imperfections; in this region, a fully atomistic description is necessary to capture the physics of deformation. The second region consists of those atoms which remain relatively unperturbed from their equilibrium positions; in this region, a fully atomistic description is unnecessary, and continuum mechanics are sufficient to describe the behavior of this portion of the lattice. Because the group harmonic behavior of the lattice is well-represented using continuum mechanics principles, the remainder of this section will summarize the methodology used to eliminate those fine scale degrees of freedom which we assume to interact harmonically; we note that the overlaying continuum is allowed to deform nonlinearly in all parts of the domain. The overall goal of this elimination is shown in Fig. 1.

The process of eliminating the unnecessary fine scale degrees of freedom will result in a modified MD equation of motion including an external force, termed the impedance force, which is a function of a damping matrix $\boldsymbol{\beta}(t)$, or equivalently its time derivative $\boldsymbol{\theta}(t)$, known as the time history kernel. The damping kernel was first derived analytically by Adelman and Doll [10] for a harmonic one-dimensional lattice, and calculated numerically in multiple dimensions by Cai et al. [11], and E and Huang [12]. The effect of the damping matrix is to dissipate high frequency energy into the eliminated degrees of freedom, resulting in a non-reflecting MD boundary condition.

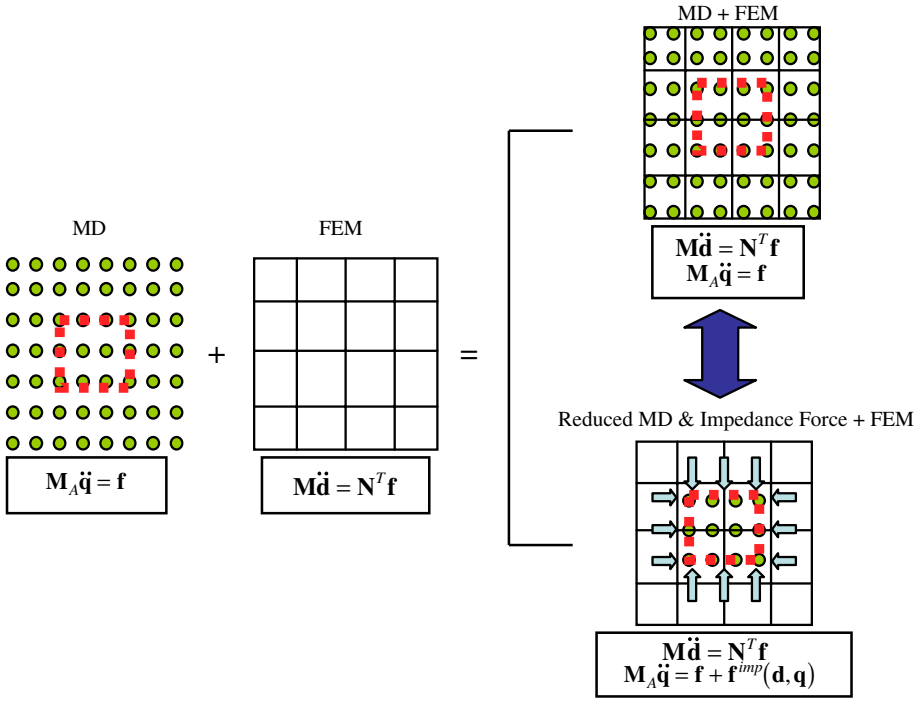

Fig. 1. Removal of redundance of FE equation of motion by elimination of unnecessary MD degrees of freedom.

The approach taken here differs from previous work; the key to the following process is the recognition that crystalline lattice structures are inherently periodic and repetitive in nature. The salient feature which results from the periodic structure is that the resulting time history kernel matrix $\boldsymbol{\theta}(t)$ has a compact size, corresponding to the minimum number of degrees of freedom in each repetitive unit cell. The periodicity of lattice structures as related to deriving non-reflecting MD boundary conditions was explored by Karpov et al. [24], and later by Wagner et al. [13], Karpov et al. [14] and Karpov et al. [15]. This approach was generalized in the context of two-dimensional multiple scale simulations by Park et al. [9]; the present work extends the approach in [9] to three-dimensional multiple scale simulations.

The first step in this process is to linearize the MD equation of motion (11), while using the equality of $\mathbf{q}$ and $\mathbf{u}$ to obtain

$$\mathbf{M}_A\ddot{\mathbf{q}} = \mathbf{M}_A\ddot{\bar{\mathbf{u}}} + \mathbf{M}_A\ddot{\mathbf{u}}' = \mathbf{f}(\bar{\mathbf{u}}) + \mathbf{K}\mathbf{u}', \tag{14}$$

where

$$\mathbf{K} = \left.\frac{\partial \mathbf{f}}{\partial \mathbf{u}}\right|_{\mathbf{u}'=0}. \tag{15}$$

The analytic solution for the time history kernel $\boldsymbol{\theta}(t)$ requires a matrix inverse of $\mathbf{K}$, as detailed in Adelman and Doll [10]. However, $\mathbf{K}$ is of size proportional to the number of MD degrees of freedom which are to be eliminated; this number is generally on the order of millions or billions, and explains why analytic solutions for $\boldsymbol{\theta}(t)$ are intractable above one dimension.

The goal in performing the linearization is to decompose the MD equation of motion into coarse and fine scale components. In doing so, we will work exclusively with the fine scale equation such that we can achieve our stated goal of limiting the fine scale to a small region of the domain, while keeping the coarse scale everywhere in the domain. We make one major assumption in our derivation, which is:

- We assume that we can write the fine scale equation of motion neglecting contributions from the coarse scale

This assumption is justified by the orthogonality of the coarse and fine scales, and also because the coarse scale time scale is much larger than that of the fine scale, which is on the order of the atomic vibrational period. Thus, we write the scale decomposed coarse and fine scale portions of the MD equation of motion as:

$$\mathbf{M}_A\ddot{\bar{\mathbf{u}}} = \mathbf{f}(\bar{\mathbf{u}}), \tag{16}$$

$$\mathbf{M}_A\ddot{\mathbf{u}}' = \mathbf{K}\mathbf{u}'. \tag{17}$$

The fine scale portion of the MD equation of motion (17) constitutes the major result of this section, and will be utilized in the following section to eliminate the unnecessary fine scale degrees of freedom.

3.2. Elimination of unnecessary fine scale degrees of freedom

We now generalize the ideas presented in the previous sections to three dimensions. The periodic lattice consists of unit cells which are repeated in three directions. Each repeated cell has n_a atoms, each of which can move in n_{SD} spatial directions. The total number of degrees of freedom in each unit cell is then $n_{\mathrm{dof}} = n_a \times n_{\mathrm{SD}}$. Each unit cell can be labeled with three indices, l, m and n, indicating the position along axes in the direction of the three primitive vectors of the crystal structure.

A two-dimensional example of a hexagonal lattice structure utilizing the unit cell numbering convention is shown in Fig. 2. In this example, the integer triplet in each cell gives the (l,m,n) coordinates; $n = 0$ for this

two-dimensional lattice. In a three-dimensional lattice, each value of n describes a plane of atoms which is bounded by x–y planes. We note that while the summation in (18) below goes over all possible lattice sites, clearly there will be many integer triplets (l,m,n) which do not describe an atomic position. In these cases, the stiffness coefficient $\mathbf{K}$ is simply zero, implying that no contribution is made to the internal force by an unoccupied lattice position.

Eq. (17) can thus be re-written as, for a three-dimensional lattice and including external forces

$$\ddot{\mathbf{u}}'_{l,m,n}(t) = \sum_{l'=l-1}^{l+1} \sum_{m'=m-\mu}^{m+\mu} \sum_{n'=n-\nu}^{n+\nu} \mathbf{M}_A^{-1}\mathbf{K}_{l-l',m-m',n-n'}\mathbf{u}'_{l',m',n'}(t) + \mathbf{M}_A^{-1}\mathbf{f}^{\text{ext}}_{l,m,n}(t), \tag{18}$$

where $\mathbf{f}^{\text{ext}}_{l,m,n}(t)$ is the external force acting upon unit cell (l,m,n), the constant stiffness matrices $\mathbf{K}$ relate the displacements in cell $(-l',-m',-n')$ to the forces in cell (l,m,n) and μ and ν represents the range of the forces in the m and n coordinate directions. We note that while atoms in a given slab of constant l are coupled to only neighboring cells $l-1$ and $l+1$, the coupling in the m and n coordinate directions is not limited to nearest neighbors. If longer ranged interactions are desired, this approximation can be relaxed simply by increasing the interaction range of the $\mathbf{K}$ matrices, as is shown in Park et al. [16].

The goal of this process will be to eliminate the atoms in the $l > 0$ cells by solving for them in terms of the $l \leqslant 0$ degrees of freedom and resubstituting that expression into (18). In this manner, we will avoid the explicit solution for the $l > 0$ degrees of freedom while implicitly including their effects into the remaining system dynamics.

The key step in removing the unwanted $l > 0$ fine scale degrees of freedom is in realizing that the motion of the boundary ($l = 0$) atoms can be caused either by the displacements of the atoms to be kept, or by an external force acting upon the boundary atoms. Therefore, it will be assumed that the motion of the boundary atoms is in fact caused by the external force which acts only at $l = 0$

$$\mathbf{f}^{\text{ext}}_{l,m,n}(t) = \delta_{l,0}\mathbf{f}^{\text{ext}}_{0,m,n}(t). \tag{19}$$

The derivation begins by taking a Laplace transform (LT) and discrete Fourier transform (DFT) of (18), giving

$$s^2\hat{\mathbf{U}}'(p,q,r,s) - s\hat{\mathbf{u}}'(p,q,r,0) - \hat{\dot{\mathbf{u}}}'(p,q,r,0) = \hat{\mathbf{A}}(p,q,r)\hat{\mathbf{U}}'(p,q,r,s) + \mathbf{M}_A^{-1}\hat{\mathbf{F}}_0^{\text{ext}}(q,r,s), \tag{20}$$

where p, q and r correspond to spatial indices l, m and n, the hatted notation indicates the discrete Fourier transform and Laplace transformed variables are indicated by the transformed variable s. $\hat{\mathbf{A}}(p,q,r)$ is the

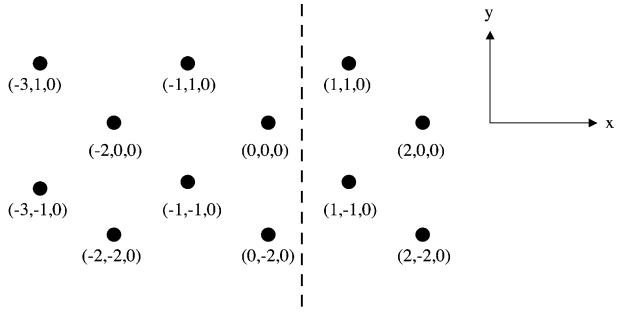

Fig. 2. Periodic two-dimensional hexagonal lattice structure numbered using unit cell nomenclature. The solid line represents the boundary between the MD region to be simulated (left), and the MD region to be eliminated (right).

Fourier transform of $\mathbf{M}_A^{-1}\mathbf{K}_{l,m,n}$. A summary of the important Laplace and Fourier transform operations utilized in this section is given in Appendix A.

Eq. (20) can be solved to give the Laplace transformed/discrete Fourier transformed displacements in terms of the external force

$$\hat{\mathbf{U}}'(p,q,r,s) = \hat{\mathbf{G}}(p,q,r,s)\left(\mathbf{M}_A^{-1}\hat{\mathbf{F}}_0^{\text{ext}}(q,r,s) + s\hat{\mathbf{u}}'(p,q,r,0) + \hat{\dot{\mathbf{u}}}'(p,q,r,0)\right), \tag{21}$$

where

$$\hat{\mathbf{G}}(p,q,r,s) = \left(s^2\mathbf{I} - \hat{\mathbf{A}}(p,q,r)\right)^{-1}. \tag{22}$$

Taking the inverse Fourier transform of (21) in the x direction gives the displacement in the x direction at atomic position l

$$\tilde{\mathbf{U}}_l'(q,r,s) = \mathbf{M}_A^{-1}\tilde{\mathbf{G}}_l(q,r,s)\hat{\mathbf{F}}_0^{\text{ext}}(q,r,s) + \tilde{\mathbf{R}}_l^d(q,r,s), \tag{23}$$

where

$$\tilde{\mathbf{R}}_l^d(q,r,s) = s\sum_{l'=-L/2+1}^{L/2}\tilde{\mathbf{G}}_{l-l'}(q,r,s)\mathbf{U}_{l'}'(q,r,0) + \sum_{l'=-L/2+1}^{L/2}\tilde{\mathbf{G}}_{l-l'}(q,r,s)\dot{\mathbf{U}}_{l'}'(q,r,0). \tag{24}$$

Here, the tilde notation implies mixed Fourier images, which depend on both the original and transform values.

Eq. (24) is typically called the random component of the displacement; this is because it depends upon the initial conditions of the eliminated degrees of freedom, which randomly depend upon the temperature. The randomness of the initial conditions occurs because they are calculated from a temperature-dependent distribution function, typically the Maxwell–Boltzmann distribution in MD simulations. Further details on this term are given in the discussion later in this section.

By writing (23) for both $l = 0$ and $l = 1$, we can obtain the displacements $\tilde{\mathbf{U}}_1'$ in terms of $\tilde{\mathbf{U}}_0'$, thereby eliminating $\hat{\mathbf{F}}_0^{\text{ext}}$ and obtaining

$$\tilde{\mathbf{U}}_1'(q,r,s) = \tilde{\mathbf{Q}}(q,r,s)\left(\tilde{\mathbf{U}}_0'(q,r,s) - \tilde{\mathbf{R}}_0^d(q,r,s)\right) + \tilde{\mathbf{R}}_1^d(q,r,s), \tag{25}$$

where

$$\tilde{\mathbf{Q}}(q,r,s) = \tilde{\mathbf{G}}_1(q,r,s)\tilde{\mathbf{G}}_0^{-1}(q,r,s). \tag{26}$$

By inverting the Fourier transform in (25) and using the convolution property of the DFT, we get

$$\mathbf{U}_{1,m,n}'(s) = \sum_{m'=-M/2+1}^{M/2}\sum_{n'=-N/2+1}^{N/2}\mathbf{Q}_{m-m',n-n'}(s)\left(\mathbf{U}_{0,m',n'}'(s) - \mathbf{R}_{0,m',n'}^d(s)\right) + \mathbf{R}_{1,m,n}^d(s), \tag{27}$$

where the random component of the displacements $\mathbf{R}_{l,m,n}^d(s)$ acting upon plane l is

$$\begin{aligned}\mathbf{R}_{l,m,n}(s) = {} & s\sum_{l'=-L/2+1}^{L/2}\sum_{m'=-M/2+1}^{M/2}\sum_{n'=-N/2+1}^{N/2}\tilde{\mathbf{G}}_{l-l',m-m',n-n'}(s)\mathbf{U}_{l',m',n'}'(0) \\ & + \sum_{l'=-L/2+1}^{L/2}\sum_{m'=-M/2+1}^{M/2}\sum_{n'=-N/2+1}^{N/2}\tilde{\mathbf{G}}_{l-l',m-m',n-n'}(s)\dot{\mathbf{U}}_{l',m',n'}'(0),\end{aligned} \tag{28}$$

where L, M and N are the number of unit cells in the x-, y- and z-directions, respectively. Eq. (27) becomes useful when it is recalled that the linearized forces acting on layer $l = 0$ due to layer $l = 1$ can be written as, recalling (18)

$$\mathbf{F}^{1\to 0}_{m,n}(s) = \sum_{m'=m-\mu}^{m+\mu} \sum_{n'=n-v}^{n+v} \mathbf{K}_{-1,m-m',n-n'} \mathbf{U}'_{1,m',n'}(s). \tag{29}$$

Substituting (27) into (29) and taking the inverse Laplace transform, the force boundary condition of the layer $l = 1$ atoms acting upon the layer $l = 0$ atoms becomes

$$\mathbf{f}^{1\to 0}_{m,n}(t) = \sum_{m'=-M/2+1}^{M/2} \sum_{n'=-N/2+1}^{N/2} \int_0^t \boldsymbol{\theta}_{m-m',n-n'}(t-\tau)\left(\mathbf{u}'_{0,m',n'}(\tau) - \mathbf{R}^d_{0,m',n'}(\tau)\right) \mathrm{d}\tau + \mathbf{R}^f_{0,m,n}(t), \tag{30}$$

where the time history kernel $\boldsymbol{\theta}$ is defined to be

$$\boldsymbol{\theta}_{m,n}(t) = \mathscr{L}^{-1}(\boldsymbol{\Theta}_{m,n}(s)), \tag{31}$$

$$\boldsymbol{\Theta}_{m-m',n-n'}(s) = \sum_{m'=m-\mu}^{m+\mu} \sum_{n'=n-v}^{n+v} \mathbf{K}_{-1,m-m',n-n'} \mathbf{Q}_{m',n'}(s), \tag{32}$$

and the random force $\mathbf{R}^f_{0,m,n}(t)$ is defined to be

$$\mathbf{R}^f_{0,m,n}(t) = \sum \sum_{m'=m-\mu}^{m+\mu} \sum_{n'=n-v}^{n+v} \mathbf{K}_{-1,m-m',n-n'} \mathbf{R}^d_{1,m',n'}(t). \tag{33}$$

As can be seen, the exact evaluation of the first term on the right-hand side of (30) requires a summation over all other unit cells along the boundary. Clearly, it would be computationally inefficient to perform the exact summation in practice, particularly if the lattice is large. Therefore, we rewrite (30) as

$$\mathbf{f}^{1\to 0}_{m,n}(t) = \sum_{m'=m-m_c}^{m_c} \sum_{n'=n-n_c}^{n_c} \int_0^t \boldsymbol{\theta}_{m-m',n-n'}(t-\tau)\left(\mathbf{u}'_{0,m',n'}(\tau) - \mathbf{R}^d_{0,m',n'}(\tau)\right) \mathrm{d}\tau + \mathbf{R}^f_{0,m,n}(t), \tag{34}$$

where n_c and m_c refer to a maximum number of atomic neighbors which will be used to compute the impedance force, which we define to be the first term on the right-hand side of (34). In the numerical examples presented later, n_c and m_c are taken to be zero, meaning that the impedance force acting upon a boundary atom depends only on the displacements of the same boundary atom. Now, the fine scale equation of motion (18) for the boundary $l = 0$ atoms can be rewritten as

$$\ddot{\mathbf{u}}'_{0,m,n} = \mathbf{A}_{0,m,n}\mathbf{u}'_{0,m,n} + \mathbf{M}_A^{-1} \sum_{m'=m-m_c}^{m_c} \sum_{n'=n-n_c}^{n_c} \int_0^t \boldsymbol{\theta}_{m-m',n-n'}(t-\tau)\left(\mathbf{u}'_{0,m',n'}(\tau) - \mathbf{R}^d_{0,m',n'}(\tau)\right) \mathrm{d}\tau + \mathbf{M}_A^{-1}\mathbf{R}^f_{0,m,n}(t). \tag{35}$$

Note that the time history kernel $\boldsymbol{\theta}(t)$ on the right-hand side of (35) contains the implicit effects of the $l > 0$ cells which have been eliminated. Adding (35) and (16), using the equality of $\mathbf{q}$ and $\mathbf{u}$ and noting that

$$\mathbf{M}_{A0}^{-1}\mathbf{f}_{0,m,n}(\bar{\mathbf{u}}) + \mathbf{A}_{0,m,n}\mathbf{u}'_{0,m,n} = \mathbf{M}_{A0}^{-1}\mathbf{f}_{0,m,n}, \tag{36}$$

where $\mathbf{M}_{A0}$ is a diagonal matrix containing the masses of the boundary ($l = 0$) atoms, we obtain the modified equation of motion for the boundary atoms which does not involve any unknown $l > 0$ degrees of freedom

$$\mathbf{M}_{A0}\ddot{\mathbf{q}}_{0,m,n}(t) = \mathbf{f}_{0,m,n}(t) + \sum_{m'=m-m_c}^{m_c}\sum_{n'=n-n_c}^{n_c}\int_0^t \boldsymbol{\theta}_{m-m',n-n'}(t-\tau)\left(\mathbf{u}'_{0,m',n'}(\tau) - \mathbf{R}^d_{0,m',n'}(\tau)\right)\mathrm{d}\tau + \mathbf{R}^f_{0,m,n}(t). \quad (37)$$

The final step to writing the MD equations of motion for the boundary atoms is to note that the fine scale component of the MD displacements can be written as

$$\mathbf{u}'_{0,m',n'}(\tau) = \mathbf{q}_{0,m',n'}(\tau) - \bar{\mathbf{u}}_{0,m',n'}(\tau). \quad (38)$$

The final form for the coupled MD and FE equations of motion thus can be written as

$$\mathbf{M}_A\ddot{\mathbf{q}}(t) = \mathbf{f}(t) + \mathbf{f}^{\mathrm{imp}}_{0,m,n}(t) + \mathbf{R}^f_{0,m,n}(t), \quad (39)$$

$$\mathbf{M}\ddot{\mathbf{d}} = \mathbf{N}^{\mathrm{T}}\mathbf{f}(\mathbf{u}), \quad (40)$$

where

$$\mathbf{f}^{\mathrm{imp}}_{0,m,n}(t) = \sum_{m'=m-m_c}^{m_c}\sum_{n'=n-n_c}^{n_c}\int_0^t \boldsymbol{\theta}_{m-m',n-n'}(t-\tau)\left(\mathbf{q}_{0,m',n'}(\tau) - \bar{\mathbf{u}}_{0,m',n'}(\tau) - \mathbf{R}^d_{0,m',n'}(\tau)\right)\mathrm{d}\tau, \quad (41)$$

Eq. (39)–(41) represent the major results of this section. With these key equations having been derived, several remarks are in order:

(i) The first Eq. (39) defines the modified MD equation of motion. The additional terms on the right-hand side of (39) result from the elimination of the fine scale degrees of freedom; the meaning of these terms is discussed in detail below. The first term on the right-hand side of (39), $\mathbf{f}(t)$, is just the standard nonlinear interatomic force that is calculated in the MD simulation. It is important to note that this force is the standard nonlinear interatomic force; the assumption of linearity was only used in describing the motion of the $l > 0$ cells which were eliminated. Specifically, the assumption of linearity manifests itself in the time history kernel $\boldsymbol{\theta}(t-\tau)$.

(ii) The second term on the right-hand side of (39), the impedance force $\mathbf{f}^{\mathrm{imp}}_{0,m,n}(t)$, contains the time history kernel $\boldsymbol{\theta}(t-\tau)$, and acts to dissipate fine scale energy from the MD simulation into the surrounding continuum. It is important to note that this force acts only on the boundary MD atoms. The numerical result is a non-reflecting boundary between the MD and FE regions, as the time history kernel dissipates away short wavelengths that cannot be represented by the surrounding continuum. Furthermore, the dependence of the impedance force on the coarse scale solution $\bar{\mathbf{u}}_{0,m',n'}(\tau)$ indicates a two-way coupled MD equation of motion, i.e., that coarse scale information originating in the continuum can be passed to the MD region. This will prove essential in later numerical examples, where the boundary conditions are applied to the surrounding continuum.

(iii) The revised MD equation of motion contains both a random displacement $\mathbf{R}^d_{0,m',n'}(t)$ and a random external force $\mathbf{R}^f_{0,m,n}(t)$. These are thermally motivated terms which arise due to the fact that the thermal effects of the eliminated fine scale degrees of freedom must be kept on the reduced MD domain, and again act *only* on the boundary atoms. These terms are considered stochastic due to the infinite number of initial conditions which are possible based on the temperature of the eliminated degrees of freedom; the existence of these terms indicates that the bridging scale method can be considered a coupled finite temperature method. Techniques for applying this stochastic force were proposed by [10]. In the examples presented in this paper, we neglect the random terms, indicating that the temperature of the surrounding continuum is 0 K. However, three of the current authors have developed a method to apply the random displacement and force; this work will be presented in a separate paper [25].

(iv) We note that the time history kernel $\boldsymbol{\theta}(t)$ is a 3×3 matrix, corresponding to the minimum number of degrees of freedom in each unit cell. The compact size of $\boldsymbol{\theta}(t)$ distinguishes this approach from other methods, such as that of Cai et al. [11]. Furthermore, once the $\mathbf{K}$ matrices have been determined, the time history kernel $\boldsymbol{\theta}(t)$ can be calculated using an automated numerical procedure, as detailed in the work of Wagner et al. [13]. This is in contrast to the work of E and Huang [12], in which the geometry of the lattice explicitly enters the formulation in determining which angles of incidence along the MD boundary it is desirable to minimize reflection for. Moreover, it is unclear how all angles of incidence can then be easily represented within the context of the E and Huang approach. The small size of $\boldsymbol{\theta}(t)$ enables us to achieve large computational savings by eliminating large portions of the lattice where an explicit atomistic representation is not desired. Specifically, even as the number of eliminated fine scale degrees of freedom grows, the size of $\boldsymbol{\theta}(t)$ remains constant, leading to computational scalability.

(v) In order to ensure that the reduced atomistic system does not relax due to spurious free surface effects, ghost atoms, or those atoms whose displacements are not determined by integrating the MD equation of motion, are utilized in the simulation. The positions of the ghost atoms are instead determined using the finite element shape functions, which is identical to that adopted to control the motion of the pad, or ghost atoms in [3].

4. Staggered time integration and coarse scale internal force

Two issues which require attention to complete the discussion about the bridging scale theory are the subjects of staggered time integration, and the calculation of the coarse scale internal force where the MD region has been eliminated.

Due to the fact that the coarse scale need not be meshed down to the MD atomic spacing, the FE equation of motion can be integrated using a larger time step than the MD simulation. This process is termed subcycling, or staggered time integration. Furthermore, standard time integrators can be used for the FE and MD simulations; the velocity verlet algorithm is used to update the MD simulation, while the explicit central-difference method is used to update the FE simulation. Details can be found in the works of Wagner and Liu [8], Park and Liu [17] and Park et al. [9].

The issue regarding the coarse scale internal force (i.e., the $N^{\mathrm{T}}\mathbf{f}(\mathbf{u})$ term in (12)) is that in the region of the domain from which the MD degrees of freedom have been eliminated, the question arises on how to evaluate $\mathbf{N}^{\mathrm{T}}f(\mathbf{u})$, because the MD internal force $\mathbf{f}(\mathbf{u})$ is not available. Due to the desire to use the same interatomic potential to calculate the internal forces even in the absence of the MD region, the Cauchy–Born rule, similar to that utilized in the quasicontinuum method [1] is used. Again, details regarding the application of the Cauchy–Born rule to the bridging scale can be found in the works of Wagner and Liu [8], and Park and Liu [17]. Further details on the Cauchy–Born rule can be found in the work of Tadmor et al. [1] and Klein and Gao [26].

We close by noting that the Cauchy–Born rule is not the only available method to calculate the internal force in the absence of the MD internal forces; recently, a virtual atom cluster (VAC) model has been proposed by Qian et al. [21,27] which does not require a hyperelastic stress update. Therefore, the bridging scale method retains applicability to many interesting structures, including carbon nanotubes.

5. Numerical example: three-dimensional dynamic crack propagation

In this section, we show numerical examples for the bridging scale in three-dimensions. Specifically, we validate the method on dynamic crack propagation within an FCC crystal. For the MD simulation, we

utilize the Lennard-Jones (LJ) 6-12 potential, though with a slightly altered form. The LJ potential we utilize contains a smooth cut-off, such that the revised potential takes the form

$$\Phi(r_{ij}) = \Phi_{\mathrm{LJ}}(r_{ij}) - \Phi_{\mathrm{LJ}}(r_c) - (r_{ij} - r_c)\Phi'_{\mathrm{LJ}}(r_c), \tag{42}$$

where $\Phi_{\mathrm{LJ}}(r_{ij})$ is the standard, unshifted LJ 6–12 potential which is a function of the distance r_{ij} between two atoms i and j, $\Phi'_{\mathrm{LJ}}(r_c)$ is the derivative of the unshifted LJ potential evaluated about the shifted distance r_c and the shifted distance r_c is defined to be

$$r_c = \alpha\sigma. \tag{43}$$

The shifted LJ potential described in (42) has a smooth cut-off in both the force and energy at the value $r_{ij} = \alpha$. For this shifted LJ potential, we utilize parameter values $\sigma = \epsilon = 1$, $\alpha = 1.50$; all atomic masses are taken to be unity.

The dynamic fracture problem schematic is shown in Fig. 3. As is shown, the specimen under consideration is covered by finite elements everywhere, while the atomistic region is confined to the central region of the cube. A pre-crack is specified in the atomistic region by prescribing that two adjacent planes of atoms do not interact, and the crack opens naturally in a mode-I type failure under the tensile ramp velocity loading shown in Fig. 4. The normalized velocity applied to the top and bottom FE surfaces was taken to be $V_{\max} = .035$.

We note that the pre-crack is initially fully contained within the interior of the MD domain; the interactions between the crack and the surfaces shown later result from the propagation of the crack. A visual image of the pre-crack is given in Fig. 5. For visualization purposes, the images in this section only display those atoms whose potential energy is greater than 90% of the equilibrium value; this technique is useful for highlighting the defective parts of the lattice which may be of interest in fracture and failure simulations.

The simulations were run using nearest neighbor atomic interactions; the bridging scale simulation employed 1024 eight-node hexahedral finite elements and 117,121 atoms, while the full MD simulation was comprised of 225,121 atoms. Different time steps were used for both simulations; the MD time step was taken to be $\Delta t_{\mathrm{md}} = .014$, and 20 MD time steps were run for each FEM time step. The MD impedance force (41) was applied to the top and bottom planes of the reduced MD region as shown in Fig. 3. All other boundary faces of the reduced MD region were taken to be free surfaces. The numerical examples shown in this paper were performed using the Sandia-developed simulation code Tahoe [28].

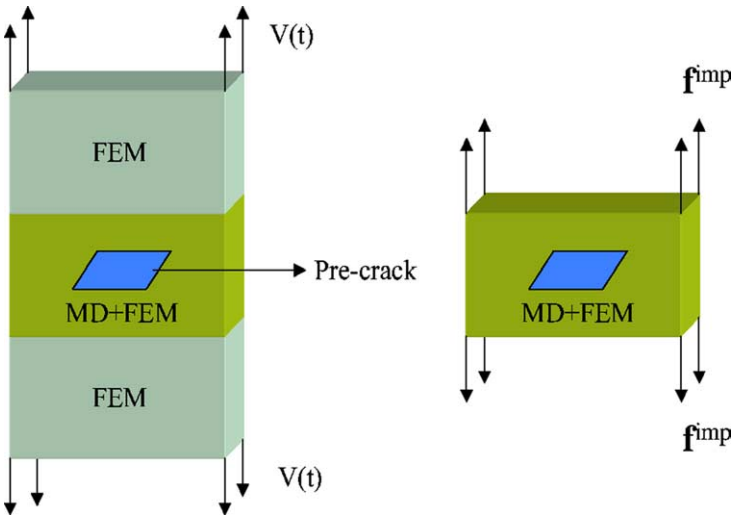

Fig. 3. Left: Schematic of 3D bridging scale crack propagation example. Right: Application of MD impedances forces (41) to top and bottom (001) planes of reduced MD domain.

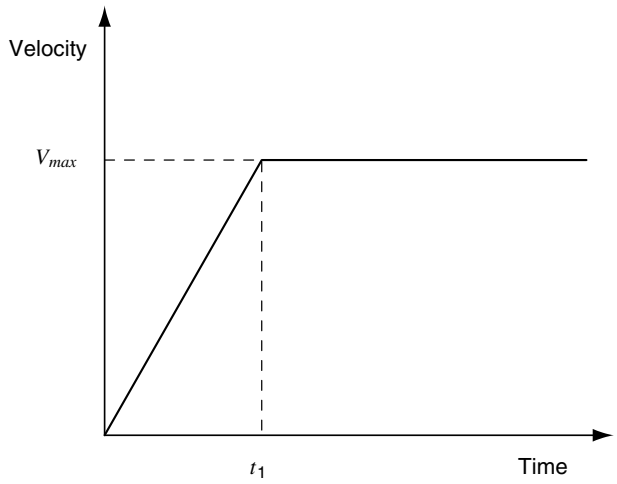

Fig. 4. Description of ramp velocity boundary condition applied to FEM.

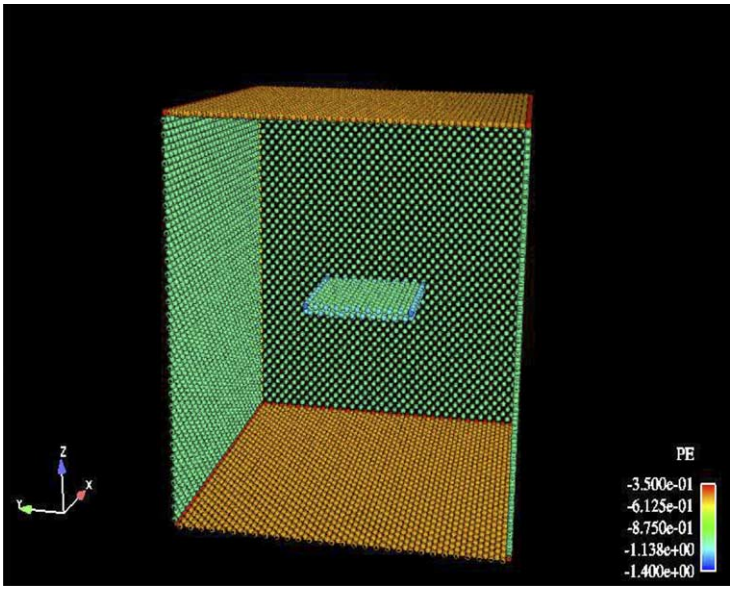

Fig. 5. Initial pre-crack for dynamic crack propagation example. Contours of potential energy shown. Only those atoms with potential energy greater than 90% of the equilibrium value are shown.

The time history kernel $\boldsymbol{\theta}(t)$ was numerically calculated for an FCC lattice structure and the shifted LJ potential for the (0 0 1) plane of atoms. The 3×3 $\boldsymbol{\theta}(t)$ matrices in (41) for the top and bottom surfaces of the reduced MD region in Fig. 3 are related as

$$\begin{pmatrix} \boldsymbol{\theta}_{11}^{\mathrm{top}}(t) & \boldsymbol{\theta}_{12}^{\mathrm{top}}(t) & \boldsymbol{\theta}_{13}^{\mathrm{top}}(t), \\ \boldsymbol{\theta}_{21}^{\mathrm{top}}(t) & \boldsymbol{\theta}_{22}^{\mathrm{top}}(t) & \boldsymbol{\theta}_{23}^{\mathrm{top}}(t), \\ \boldsymbol{\theta}_{31}^{\mathrm{top}}(t) & \boldsymbol{\theta}_{32}^{\mathrm{top}}(t) & \boldsymbol{\theta}_{33}^{\mathrm{top}}(t), \end{pmatrix} = \begin{pmatrix} \boldsymbol{\theta}_{11}^{\mathrm{bot}}(t) & \boldsymbol{\theta}_{12}^{\mathrm{bot}}(t) & -\boldsymbol{\theta}_{13}^{\mathrm{bot}}(t), \\ \boldsymbol{\theta}_{21}^{\mathrm{bot}}(t) & \boldsymbol{\theta}_{22}^{\mathrm{bot}}(t) & -\boldsymbol{\theta}_{23}^{\mathrm{bot}}(t), \\ -\boldsymbol{\theta}_{31}^{\mathrm{bot}}(t) & -\boldsymbol{\theta}_{32}^{\mathrm{bot}}(t) & \boldsymbol{\theta}_{33}^{\mathrm{bot}}(t) \end{pmatrix}. \tag{44}$$

Similar relationships relating the $\boldsymbol{\theta}(t)$ matrices for opposite faces of the FCC cube can also be determined.

Fig. 6 shows the diagonal components of $\boldsymbol{\theta}(t)$ in 3D with $n_c = 0$ and $m_c = 0$. As can be seen, $\boldsymbol{\theta}_{33}(t)$ is the most important component to consider in the calculations, while $\boldsymbol{\theta}_{11}(t) = \boldsymbol{\theta}_{22}(t)$. We neglect higher order values of $\boldsymbol{\theta}(t)$ corresponding to $n_c > 0$ and $m_c > 0$ as those values for $\boldsymbol{\theta}(t)$ are at most 10% of the values shown in Fig. 6.

The ability of the impedance force (41) to dissipate high frequency MD energy for $n_c = 0$ was demonstrated in the two-dimensional work of Park et al. [9]; setting $n_c = 0$ and $m_c = 0$ in (41) also leads to maximum computational efficiency. The three-dimensional time history kernel exhibits many of the salient features seen in the two-dimensional time history kernels for the LJ potential [9], specifically the quick decay in the amplitude of $\boldsymbol{\theta}(t)$, which allows the truncation of the kernels after short time durations.

A comparison between the bridging scale simulation and the full MD simulation is given in four distinct snapshots, which chronicle the time history of the crack propagation. For clarity, the figures show a comparison between the reduced MD region in the bridging scale simulation and that portion of the full MD domain that corresponds to that simulated using the bridging scale.

In the first snapshot seen in Fig. 7, the initially square pre-crack has evolved under loading to resemble a penny-shaped crack. Fig. 7 shows the crack just before propagation initiates; this figure and all subsequent figures show contours of potential energy, while the atomic displacements have been magnified by a factor of five for easy viewing.

After the crack propagation has initiated and the crack nears the surfaces of the MD domain, the onset and subsequent branching of the crack is seen in Figs. 8 and 9. In this simulation, it is important to note that the branching is a surface effect, i.e., the branching is caused when the crack front approaches the free surface. The branching is caused by a lack of constraint as the crack approaches the surface; in essence, a truly mode-I type loading does not exist near the surface, hence the crack is not constrained to propagate directly through the surface, and instead branches to cause material failure.

The final configurations of the bridging scale simulation and the full MD simulation are shown in Fig. 10. Again, the bridging scale simulation matches the full MD simulation well, including the final configuration of the crack branches, and potential energy. We note that the crack initiation time and position of the crack and its branches during propagation appear to correctly match the results of the full MD sim-

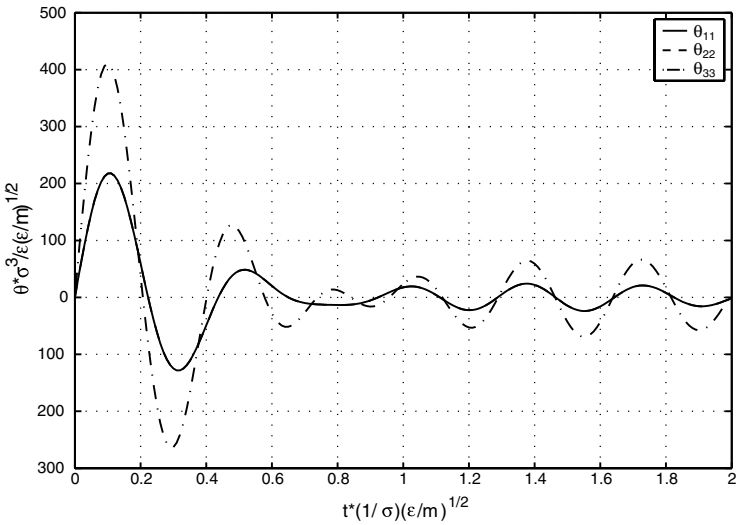

Fig. 6. Components of $\boldsymbol{\theta}(t)$ for 3D FCC lattice interacting via Lennard-Jones 6–12 potential.

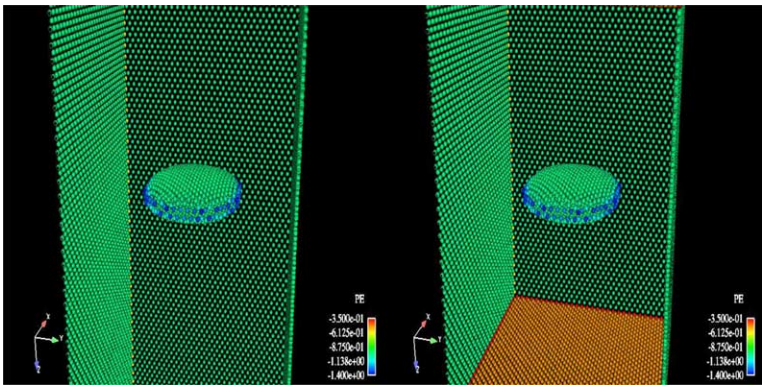

Fig. 7. Onset of crack growth for (left) full MD simulation and (right) bridging scale simulation.

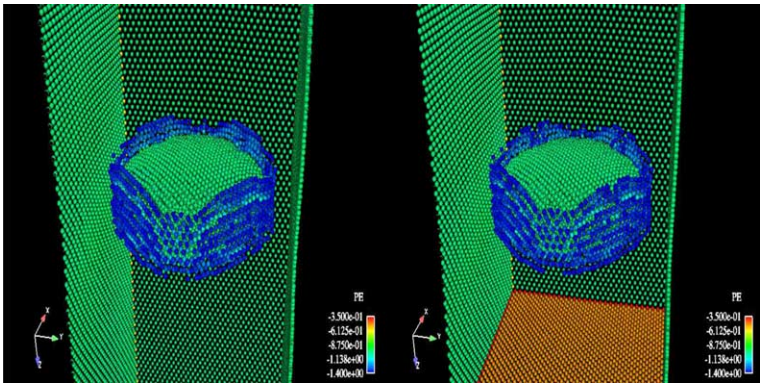

Fig. 8. Onset of crack branching in (left) full MD simulation and (right) bridging scale simulation.

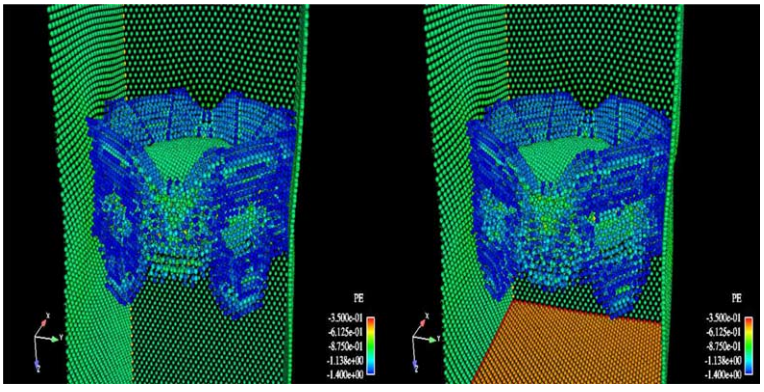

Fig. 9. Out of plane crack branching for (left) full MD simulation and (right) bridging scale simulation.

ulation, as measured visually. Unlike the two-dimensional multiple scale simulations of dynamic fracture considered by the same authors [9], the crack tip position has not been detailed as a function of time, due to the inherent difficulty in tracking a branching crack front in three dimensions.

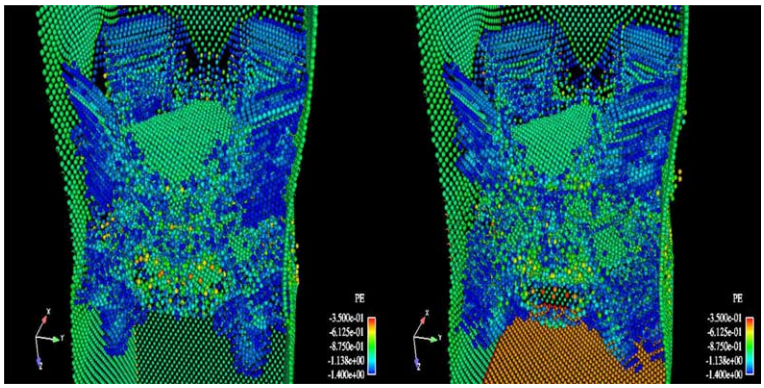

Fig. 10. Final crack configuration in (left) full MD simulation and (right) bridging scale simulation.

Fig. 11 shows the deformed FE mesh within the coupled MD/FE region after the crack branches have reached the MD domain boundaries. The extreme distortion of the elements at the surface which contain a crack branch can be seen. We note that the finite elements within the coupled MD/FE region can sustain deformations not typically allowed by standard finite elements due to the fact that the internal forces for those elements are only a function of the underlying MD forces, as in (40). In other words, no constitutive relationship which requires the calculation of inverse Jacobian mappings is needed for these elements, allowing them to deform along with the underlying lattice structure. This extreme deformation of finite elements was also noted in the two-dimensional multiple scale work of Park et al. [9].

In comparing the computational time for the full MD and bridging scale simulations, the bridging scale simulation took about 76% of the time for the full MD simulation. While the computational time was indeed reduced, it was not reduced by half, as might be expected; the ideal value of half could only be achieved were there exactly half the number of degrees of freedom in the reduced/coupled system. For the coupled system, additional computational cost is incurred for two major reasons. First, the solution of the coarse scale degrees of freedom is required. More importantly, the additional cost is due to the coupling terms between the coarse and fine scales, particularly the impedance force in (41), which requires the storage of displacement histories for both coarse and fine scales. Similar results for computational efficiency

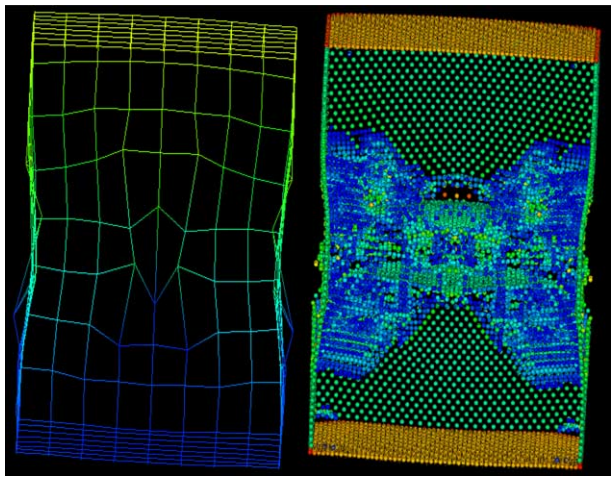

Fig. 11. Left: deformed FE mesh in coupled MD/FE region. Right: corresponding crack propagation within MD domain.

were seen in the two-dimensional work of Park et al. [9], in which it was demonstrated that computational efficiency improved as the eliminated number of MD degrees of freedom increased. This is due to the fact that the size of the time history kernel $\boldsymbol{\theta}(t)$ stays constant regardless of the number of eliminated MD degrees of freedom.

As was demonstrated in this and previous works [9,17], despite the assumption of linearity at the MD boundary, the boundary atoms are allowed to undergo large, elastic deformations. The assumption of linearity precludes the advancement of defects through the boundary; in these types of situations in which a defect or crack tip migrates to the boundary of the MD domain, an adaptive procedure is required such that the MD domain can support the long-ranged propagation of crystal defects. This is indeed the subject of current research.

However, as can be seen in this work and the two-dimensional work of Park et al. [9], despite the large displacements, the external loading on the FEM is correctly transferred to the MD region, as the crack initiates at the correct time and propagates along the correct direction, i.e., similar to the benchmark full MD simulation. This indicates that the linearized assumption still allows correct transfer of boundary conditions from the FEM to MD along with eliminating high frequency waves emitted by the propagating crack tip.

Finally, Figs. 7–10 powerfully demonstrate the utility of multiple scale methods. In these images, it is clearly seen that only a small percentage of the atoms are largely perturbed from their equilibrium positions, even during catastrophic material failure processes such as fracture. Due to the fact that only a small percentage of the atoms play a critical role in describing the onset and subsequent propagation of cracks and defects, it seems clear that multiple scale methods are well-suited to eliminate the unnecessary atomistic degrees of freedom in favor of a continuum representation, as is done here.

6. Conclusions

This paper has presented a generalization of the bridging scale concurrent method to three dimensions. Central to the generalization is the numerical calculation of the time history kernel matrix $\boldsymbol{\theta}(t)$, which acts upon the reduced MD system, and results in a non-reflecting MD boundary condition. Furthermore, the coupling of the MD equation of motion to the overlaying coarse scale allows boundary conditions that are applied to the continuum to be transferred naturally to the atomistic region. This feature is essential in multiple scale simulations, where the goal is to simulate realistic-sized problems that cannot be solved by MD alone.

In comparison to existing multiple scale methods, the bridging scale offers the following advantages. Unlike the quasicontinuum method [1], the bridging scale is valid for dynamic, finite temperature papers. Unlike the MAAD method of Abraham et al. [2], the finite element mesh need not be graded down to the atomic spacing at the MD/FEM interface. Finally, unlike the coarse-grained MD (CGMD) method of Rudd and Broughton [5], the MD equation of motion contains the correct damping term, Eq. (41), that is necessary to eliminate high frequency wave reflection at the MD/FEM boundary. This deficiency in CGMD was noted in the work of Rudd [29], but a literature search found no recent work utilizing the new formulation.

The form of the time history kernel matrix $\boldsymbol{\theta}(t)$ also offers distinct advantages to previous works. By utilizing the inherent periodicity of crystalline lattice structures, $\boldsymbol{\theta}(t)$ was shown to have a compact size, which is of the minimum number of degrees of freedom in each unit cell. Therefore, for the three-dimensional FCC lattice considered in this work, $\boldsymbol{\theta}(t)$ is a 3×3 matrix. Additional benefits to the current approach for numerically calculating $\boldsymbol{\theta}(t)$ include the fact that an automated numerical procedure involving only standard Laplace and Fourier transform techniques has been established [13], and that only the force constants $\mathbf{K}$ that describe the interactions between neighboring unit cells are needed to run the automated numerical procedure.

The bridging scale was applied to three-dimensional dynamic fracture problems in an FCC crystal. It was demonstrated that within the bridging scale calculations, characteristic physics of crack propagation such as branching are fully captured, and allowed to occur. High frequency wavelengths emitted by the propagating

crack plane as atomic bonds are broken are dissipated away by the impedance force acting on the reduced MD system. Finally, comparisons to a full MD simulation showed the accuracy of the bridging scale simulation; the energy patterns and features of the crack initiation and branching compared extremely well.

Future research on the bridging scale is currently focussed on two directions. First, the bridging scale is being extended to allow non-nearest neighbor atomic interactions using the recently developed MD boundary condition for non-nearest neighbor interactions [16]. This feature is essential in large deformation and high strain-rate physics, as demonstrated by Holian et al. [30]; it was shown in that work that the generation of defects is greatly influenced by the number of atomic interactions considered for various interatomic potentials. Even for longer-ranged interactions, the size of the time history kernel $\theta(t)$ remains the same as for nearest neighbor interactions. The computational effort to apply the impedance force does increase, as the impedance forces must be applied to multiple planes of boundary atoms commensurate with the interaction distance of the potential. However, the computational savings incurred by this method improves as the number of eliminated MD degrees of freedom increases due to the constant size of $\theta(t)$.

A related issue deals with the issue of double counting the energy at the MD/FEM interface. Such double counting of energy can lead to so-called ghost forces, in which an atomic lattice that should be at equilibrium relaxes spuriously due to additional forces on the boundary atoms [7]; these forces result from coupling a nonlocal atomistic region with a local continuum. The bridging scale does not suffer from ghost forces, as ghost atoms are utilized to ensure that atoms at the crystal boundary see a full complement of atomic neighbors. However, care must be taken to ensure that the continuum nodal forces are correctly computed when nonnearest neighbor atomic interactions are utilized. This issue has been addressed by Klein and Zimmerman [31], and will be incorporated into any bridging scale simulations which utilize long-ranged interactions.

Secondly, research is underway to incorporate a finite temperature coupling using the random, or stochastic terms $\mathbf{R}(t)$ [25]. We note that there is no limitation in the temperature that can currently be supported within the MD region; however, there is currently no method by which the energy dissipated out of the MD region by the time history kernel $\theta(t)$ is represented in the surrounding continuum. The random terms $\mathbf{R}(t)$ are needed to allow the continuum to exert a thermal dependence on the reduced MD system such that the reduced MD system remains at the desired temperature of simulation. In this manner, the performance of the bridging scale, and specifically the time history kernel $\theta(t)$, can be analyzed for anharmonic effects such as thermal expansion.

Acknowledgments

We gratefully acknowledge the support of the NSF and also the NSF-IGERT program. We like to thank the NSF Summer Institute on Nano Mechanics and Materials and the Army Research Office (ARO) for their support of this research. H.S.P. expresses his grateful thanks to the Engineering Sciences Summer Institute (ESSI) at Sandia National Laboratories. Sandia National Laboratories is supported by the US Department of Energy under Contract DE-AC04-94AL85000.

Appendix A. 3D Lennard-Jones stiffness matrices

We show here the numerically calculated $\mathbf{K}$ matrices for a 3D FCC lattice structure with nearest neighbor Lennard-Jones interactions. The schematic for a unit cell with its 12 nearest neighbors is shown in Fig. 12. For potential parameters $\sigma = \epsilon = 1$, we define the interaction coefficient k to be

$$k = 28.5725. \tag{A.1}$$

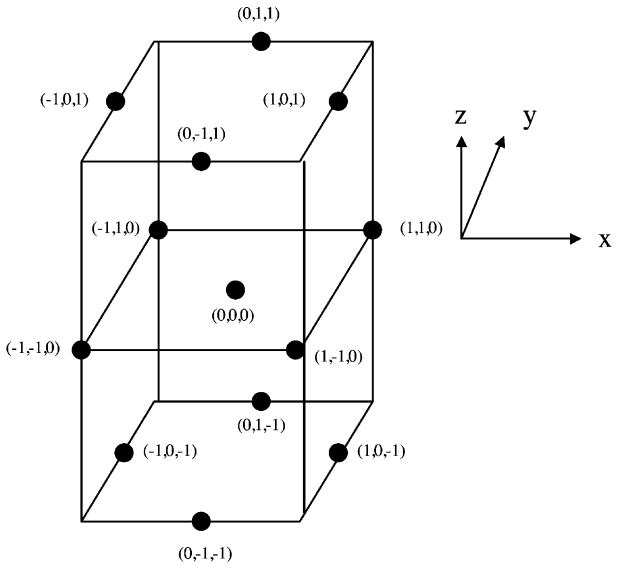

Fig. 12. Schematic of unit cell (000), and its 12 nearest neighbors for an FCC lattice.

In terms of k, the $\mathbf{K}$ matrices can be written as

$$\mathbf{K}_{0,0,0} = 8k\begin{pmatrix} -1 & 0 & 0 \\ 0 & -1 & 0 \\ 0 & 0 & -1 \end{pmatrix}, \tag{A.2}$$

$$\mathbf{K}_{1,1,0} = \mathbf{K}_{-1,-1,0} = k\begin{pmatrix} 1 & 1 & 0 \\ 1 & 1 & 0 \\ 0 & 0 & 0 \end{pmatrix}, \tag{A.3}$$

$$\mathbf{K}_{1,-1,0} = \mathbf{K}_{-1,1,0} = k\begin{pmatrix} 1 & -1 & 0 \\ -1 & 1 & 0 \\ 0 & 0 & 0 \end{pmatrix}, \tag{A.4}$$

$$\mathbf{K}_{1,0,1} = \mathbf{K}_{-1,0,-1} = k\begin{pmatrix} 1 & 0 & 1 \\ 0 & 0 & 0 \\ 1 & 0 & 1 \end{pmatrix}, \tag{A.5}$$

$$\mathbf{K}_{1,0,-1} = \mathbf{K}_{-1,0,1} = k\begin{pmatrix} 1 & 0 & -1 \\ 0 & 0 & 0 \\ -1 & 0 & 1 \end{pmatrix}, \tag{A.6}$$

$$\mathbf{K}_{0,1,1} = \mathbf{K}_{0,-1,-1} = k\begin{pmatrix} 0 & 0 & 0 \\ 0 & 1 & 1 \\ 0 & 1 & 1 \end{pmatrix}, \tag{A.7}$$

$$\mathbf{K}_{0,1,-1} = \mathbf{K}_{0,-1,1} = k\begin{pmatrix} 0 & 0 & 0 \\ 0 & 1 & -1 \\ 0 & -1 & 1 \end{pmatrix}, \tag{A.8}$$

Appendix B. Discrete Fourier transform

The discrete Fourier transform (DFT) is used to transform functions from real space to wavenumber space. Assuming that the function f can be defined at all atomic positions l, we denote the value of f and position l as f_l. The DFT of f, which is described using the hatted notation, is defined to be

$$\hat{f}(p) = \mathscr{F}_{l\to p}\{f_l\} \equiv \sum_{l=-\frac{L}{2}+1}^{\frac{L}{2}} f_l \mathrm{e}^{-\mathrm{i}2\pi pl/L}, \tag{B.1}$$

where L denotes the number of lattice sites, and p can take any integer value between $-(L/2)+1$ and $L/2$. The inverse Fourier transform (IFT) is then defined to be

$$f_l = \mathscr{F}^{-1}_{p\to l}\{\hat{f}(p)\} \equiv \frac{1}{L}\sum_{p=-\frac{L}{2}+1}^{\frac{L}{2}} \hat{f}(p)\mathrm{e}^{\mathrm{i}2\pi pl/L}. \tag{B.2}$$

We close by noting the convolution property of the DFT, i.e., that the transform of the convolution of two functions in space is equal to the product of the transforms of the individual functions

$$\mathscr{F}_{l\to p}\left(\sum_{l'=-\frac{L}{2}+1}^{\frac{L}{2}} f_{l-l'}g_{l'}\right) = \hat{f}(p)\hat{g}(p). \tag{B.3}$$

Appendix C. Laplace transform

The Laplace transform (LT) is used to transform functions of time t into the transform variable s. The LT of a function $f(t)$ is defined to be

$$F(s) = \mathscr{L}\{f(t)\} \equiv \int_0^\infty f(t)\,\mathrm{e}^{-st}\,\mathrm{d}t. \tag{C.1}$$

The inverse Laplace transform (ILT) is defined to be

$$f(t) = \mathscr{L}^{-1}\{F(s)\} \equiv \frac{1}{2\pi\mathrm{i}}\int_{c-\mathrm{i}\infty}^{c+\mathrm{i}\infty} F(s)\,\mathrm{e}^{\mathrm{st}}\,\mathrm{d}s, \tag{C.2}$$

where c is a constant greater than the real parts of all singularies of $F(s)$. We give two other important definitions for the LT, first the transform of the time derivative of a function

$$\mathscr{L}\left\{\frac{\mathrm{d}^n f(t)}{\mathrm{d}t^n}\right\} = s^n F(s) - s^{n-1}f(0) - s^{n-2}\frac{\mathrm{d}f}{\mathrm{d}t}(0) - \cdots - \frac{\mathrm{d}^{n-1}f}{\mathrm{d}t^{n-1}}(0). \tag{C.3}$$

Finally, similar to the DFT, the LT of a convolution integral of two functions is equal to the product of the transforms of the individual functions

$$\mathscr{L}\{\int_0^t f(t-\tau)g(\tau)\,\mathrm{d}\tau\} = F(s)G(s). \tag{C.4}$$

References

[1] E. Tadmor, M. Ortiz, R. Phillips, Quasicontinuum analysis of defects in solids, Philosophical Magazine A 73 (1996) 1529–1563.
[2] F.F. Abraham, J. Broughton, N. Bernstein, E. Kaxiras, Spanning the continuum to quantum length scales in a dynamic simulation of brittle fracture, Europhysics Letters 44 (1998) 783–787.
[3] L.E. Shilkrot, R.E. Miller, W.A. Curtin, Multiscale plasticity modeling: coupled atomistics and discrete dislocation mechanics, Journal of the Mechanics and Physics of Solids 52 (2004) 755–787.
[4] S.P. Xiao, T. Belytschko, A bridging domain method for coupling continua with molecular dynamics, Computer Methods in Applied Mechanics and Engineering 193 (2004) 1645–1669.
[5] R.E. Rudd, J.Q. Broughton, Coarse-grained molecular dynamics and the atomic limit of finite elements, Physical Review B 58 (1998) 5893–5896.
[6] W.K. Liu, E.G. Karpov, S. Zhang, H.S. Park, An introduction to computational nano mechanics and materials, Computer Methods in Applied Mechanics and Engineering 193 (2004) 1529–1578.
[7] W.A. Curtin, R.E. Miller, Atomistic/continuum coupling in computational materials science, Modelling and Simulation in Materials Science and Engineering 11 (2003) R33–R68.
[8] G.J. Wagner, W.K. Liu, Coupling of atomistic and continuum simulations using a bridging scale decomposition, Journal of Computational Physics 190 (2003) 249–274.
[9] H.S. Park, E.G. Karpov, P.A. Klein, W.K. Liu, The bridging scale for two-dimensional atomistic/continuum coupling, Philosophical Magazine 85 (1) (2005) 79–113.
[10] S.A. Adelman, J.D. Doll, Generalized Langevin equation approach for atom/solid-surface scattering: General formulation for classical scattering off harmonic solids, Journal of Chemical Physics 64 (1976) 2375–2388.
[11] W. Cai, M. DeKoning, V.V. Bulatov, S. Yip, Minimizing boundary reflections in coupled-domain simulations, Physical Review Letters 85 (2000) 3213–3216.
[12] W. E, Z.Y. Huang, A dynamic atomistic-continuum method for the simulation of crystalline materials, Journal of Computational Physics 182 (2002) 234–261.
[13] G.J. Wagner, E.G. Karpov, W.K. Liu, Molecular dynamics boundary conditions for regular crystal lattices, Computer Methods in Applied Mechanics and Engineering 193 (2004) 1579–1601.
[14] E.G. Karpov, G.J. Wagner, W.K. Liu, A Green's function approach to deriving non-reflecting boundary conditions in molecular dynamics simulations, International Journal for Numerical Methods in Engineering 62 (2005) 1250–1262.
[15] E.G. Karpov, H. Yu, H.S. Park, W.K. Liu, Q.J. Wang, D. Qian, Multiscale boundary conditions in crystalline solids: theory and application to nanoindentation, Physical Review B (in preparation).
[16] H.S. Park, E.G. Karpov, W.K. Liu, Non-reflecting boundary conditions for atomistic, continuum and coupled atomistic/continuum simulations, International Journal for Numerical Methods in Engineering (accepted).
[17] H.S. Park, W.K. Liu, Introduction and tutorial on multiple scale analysis in solids, Computer Methods in Applied Mechanics and Engineering 193 (2004) 1733–1772.
[18] W.K. Liu, R. Uras, Y. Chen, Enrichment of the finite element method with the reproducing kernel particle method, Journal of Applied Mechanics 64 (1997) 861–870.
[19] G.J. Wagner, W.K. Liu, Hierarchical enrichment for bridging scales and meshfree boundary conditions, International Journal for Numerical Methods in Engineering 50 (2001) 507–524.
[20] L.T. Zhang, G.J. Wagner, W.K. Liu, A parallel meshfree method with boundary enrichment for large-scale cfd, Journal of Computational Physics 176 (2002) 483–506.
[21] D. Qian, G.J. Wagner, W.K. Liu, A multiscale projection method for the analysis of carbon nanotubes, Computer Methods in Applied Mechanics and Engineering 193 (2004) 1603–1632.
[22] H.S. Park, E.G. Karpov, W.K. Liu, A temperature equation for coupled atomistic/continuum simulations, Computer Methods in Applied Mechanics and Engineering 193 (2004) 1713–1732.
[23] H. Kadowaki, W.K. Liu, Bridging multi-scale method for localization problems, Computer Methods in Applied Mechanics and Engineering 193 (2004) 3267–3302.
[24] E.G. Karpov, N.G. Stephen, D.L. Dorofeev, On static analysis of finite repetitive structures by discrete fourier transform, International Journal of Solids and Structures 39 (16) (2002) 4291–4310.
[25] E.G. Karpov, H.S. Park, W.K. Liu, D.L. Dorofeev, On the modeling of chaotic thermal motion in solids, Applied Physics Letters (submitted).

[26] P. Klein, H. Gao, Crack nucleation and growth as strain localization in a virtual-bond continuum, Engineering Fracture mechanics 61 (1) (1998) 21–48.
[27] D. Qian, R.H. Gondhalekar, A virtual atom cluster approach to the mechanics of nanostructures, International Journal for Multiscale Computational Engineering 2 (2) (2005) 277–289.
[28] Tahoe, http://tahoe.ca.sandia.gov.
[29] R.E. Rudd, Coarse-grained molecular dynamics: dissipation due to internal modes, Materials Research Society Symposium Proceedings Fall 2001 (Symposium T).
[30] B.L. Holian, A.F. Voter, N.J. Wagner, R.J. Ravelo, S.P. Chen, W.G. Hoover, C.G. Hoover, J.E. Hammerberg, T.D. Dontje, Effects of pairwise versus many-body forces on high-stress plastic deformation, Physical Review A 43 (6) (1991) 2655–2661.
[31] P.A. Klein, J.A. Zimmerman, Coupled atomistic-continuum simulation using arbitrary overlapping domains, Journal of Computational Physics (submitted).